Optoelectronic optimization of graded-bandgap thin-film AlGaAs solar cells. Part II: optimal antireflection front-surface texturing

FAIZ AHMAD[1,2], PETER B. MONK[2], AND AKHLESH LAKHTAKIA[1]

[1] The Pennsylvania State University, Department of Engineering Science and Mechanics, NanoMM–Nanoengineered Metamaterials Group, University Park, PA 16802, USA
[2] University of Delaware, Department of Mathematical Sciences, 501 Ewing Hall, Newark, DE 19716, USA

Compiled September 22, 2023

In Part I, we used a coupled optoelectronic model to optimize a thin-film AlGaAs solar cell with a *graded-bandgap photon-absorbing layer* and a *periodically corrugated Ag backreflector combined with localized ohmic Pd–Ge–Au backcontacts*, because both strategies help to improve the performance of AlGaAs solar cells. However, the results in Part I were affected by a normalization error, which came to light when we replaced the hybridizable discontinuous Galerkin scheme for electrical computation by the faster finite-difference scheme. Therefore, we re-optimized the solar cells containing an n-AlGaAs photon-absorbing layer with either (i) homogeneous, (ii) linearly graded, or (iii) nonlinearly graded bandgap. As another way to improve the power-conversion efficiency is by using surface antireflection texturing on the wavelength scale, we also optimized four different types of 1D periodic surface texturing: (i) rectangular, (ii) convex hemi-elliptical, (iii) triangular, and (iv) concave hemi-elliptical. Our new results show that the optimal nonlinear bandgap grading enhances the efficiency by as much as 3.31% when the n-AlGaAs layer is 400-nm-thick and 1.14% when that layer is 2000-nm-thick. A hundredfold concentration of sunlight can enhance the efficiency by a factor of 11.6%. Periodic texturing of the front surface on the scale of 0.5–2 free-space wavelengths provides a small relative enhancement in efficiency over the AlGaAs solar cells with planar front surface, the enhancement being lower when the n-AlGaAs layer is thicker.

http://dx.doi.org/10.1364/ao.XX.XXXXXX

1. INTRODUCTION

In a previous paper [1], hereafter referred to as Part I, we used a rigorous coupled optoelectronic model to optimize a thin-film AlGaAs photovolatic solar cell with a graded-bandgap n-AlGaAs photon-absorbing layer and a periodically corrugated Ag backreflector combined with localized ohmic Pd–Ge–Au backcontacts shown in Fig. 1(a). Both the bandgap grading of the photon-absorbing layer and the periodically corrugated backreflector with localized ohmic contacts were predicted to enhance the light-to-electricity power-conversion efficiency η.

The optoelectronic model comprises two submodels [2]: optical and electrical. The optical submodel yields the electron-hole-pair (EHP) generation rate inside the semiconductor layers of the solar cell, assuming normal illumination by unpolarized polychromatic light endowed with the AM1.5G solar spectrum. That generation rate is used in the electrical submodel as an input to the equations for the drift and diffusion of charge carriers [3, 4], the output being the current density $J_{\rm dev}$ generated by the solar cell as a function of the bias voltage $V_{\rm ext}$ under steady-state conditions.

In the electrical submodel used in Part I [1], the hybridizable discontinuous Galerkin (HDG) scheme [2, 5] was adopted to solve the drift-diffusion equations. In order to speed up electrical computation, we replaced the HDG scheme by the finite-difference method (FDM) [6] and discovered a normalization error in the code [7]. Hence, we re-optimized the AlGaAs solar cells containing an n-AlGaAs photon-absorbing layer with either (i) homogeneous, (ii) linearly graded, or (iii) nonlinearly graded bandgap. The effects of the periodically corrugated Ag backreflector with ohmic backcontacts and the optimal results

for solar cells with a homogeneous n-AlGaAs photon-absorbing layer in Part I [1] did not alter significantly. However, the effects of bandgap grading on the efficiency did change significantly, as we report here.

After correcting the normalization error, we found that the overall conclusions in that paper still hold. However, as the specifics of the reported data were impacted, we are also reporting here the revised data on AlGaAs solar cells exposed to concentrated sunlight.

Concentrated photovoltaic (CPV) systems occupy a smaller area and use less photon-absorbing semiconductor material than the conventional non-CPV systems [8], thereby reducing the levelized cost of electricity. Solar concentration can be achieved using optical concentrators to increase the intensity of sunlight incident on the solar cell's surface. However, CPV systems typically use more sophisticated and expensive multi-junction solar cells [8], the most efficient of which contain III-V semiconductors. But, III-V multi-junction solar cells are expensive because they (i) use scarce materials and (ii) require time-consuming and expensive manufacturing processes such as metal-organic vapor-phase epitaxy [9]. Bandgap grading provides a way to capture solar photons in a broader spectral regime, also the principle exploited in multi-junction III-V solar cells. Hence, optical concentration combined with bandgap grading of AlGaAs thin-film solar cells offers a cost-effective alternative to III-V multi-junction solar cells [10].

Another way to improve the efficiency of a solar cell is by increasing the front-interface transmittance and thereby enhancing photon absorption by reducing loss due to front reflection [11]. A commonplace antireflection strategy utilizes a multilayer coating comprising layers of various materials and thicknesses [12]. However, these antireflection coatings exhibit poor performance because of narrow bandwidth [13, 14]. An alternative strategy is to texture the front surface to reduce reflection in a broad spectral regime due to, in effect, a gradual variation of the refractive index along the thickness direction [15–18].

A perusal of extant literature suggests that texturing at the scale of 20–50 free-space wavelengths is effective [15, 19–27] for crystalline silicon solar cells. However, this texturing is not useful for thin-film solar cells because their thinner photon-absorbing layers are prone to having more defects due to the deep etching used for surface texturing [28]. Texturing the front surface on the scale of 0.5–2 free-space wavelengths is known to reduce reflection [11, 12, 15–17]. Hence, we optimized the geometrical parameters of the following four different types of 1D periodic surface texturing shown in Figs. 1(b) and 1(c): (i) rectangular, (ii) convex hemi-elliptical, and (iii) triangular, and (c) concave hemi-elliptical.

This paper is organized as follows. Section 2 on optoelectronic optimization is divided into two subsections. The optical description of the solar cell is presented in Sec 2.A and the electrical description in Sec. 2.B. Numerical results are presented and discussed in Sec. 3, divided into four subsections as follows. Sec. 3.A is for solar cells with a linearly graded n-AlGaAs photon-absorbing layer. Optimal results for solar cells with a nonlinearly graded-bandgap n-AlGaAs photon-absorbing layer are discussed in Sec. 3.B. Section 3.C provides the optimal results for solar cells with concentrated sunlight. Section 3.D provides the optimal results for solar cells with optimal front-surface texturing. The paper ends with some remarks in Sec. 4.

2. OPTOELECTRONIC OPTIMIZATION

A. Optical submodel

The solar-cell structure depicted in Fig. 1(a) has the following parameters fixed: $L_{MgF_2} = 110$ nm, $L_{ZnS} = 40$ nm, $L_{FSP} = 20$ nm, $L_w = 50$ nm, $L_s \in [100, 2000]$ nm, $L_{BSP} = 20$ nm, $L_{Pd} = 20$ nm, $L_{Ge} = 50$ nm, $L_{Au} = 100$ nm, and $L_{Ag} = 100$ nm. The parameters $L_x \in [100, 1000]$ nm and $\zeta \in [0.05, 1]$ were considered variable for optimization. Assuming normal illumination by unpolarized polychromatic light endowed with the AM1.5G solar spectrum, we used the rigorous coupled-wave approach [2, 29] in the optical submodel, because the solar cell is periodic along the x axis with period L_x. The thickness direction is parallel to the z axis.

In order to incorporate the surface antireflection texturing, the structure of the solar cell was modified as shown in Figs. 1(b) and 1(c). The thicknesses $L_{ZnS} \in [1, 1000]$ nm of the ZnS layer and $L_{MgF_2} \in [1, 1000]$ nm of the MgF_2 layer were considered variable for optimization. The height $L_h \in [1, 1000]$ nm of the periodic surface texturing was also considered variable for optimization for all four types of texturing: (i) rectangular, (ii) convex hemi-elliptical, (iii) triangular, and (iv) concave hemi-elliptical. In the case of rectangular texturing, the duty cycle $\zeta_h \in [0, 1]$ was also considered as an optimization parameter.

Complete details of optical calculations and the spectrums of the real and imaginary parts of the relative permittivity $\varepsilon(\lambda_0)/\varepsilon_0$ of all the materials used in our calculations are available in Part I [1] and Ref. 2. The output of the optical submodel is the x-averaged EHP generation rate $G(z)$ as a function of z inside the semiconductor layers of the solar cell.

B. Electrical submodel

The electrical description also remains unchanged from Part I [1]. However, the electrical calculation procedure changed. We used the FDM [6] instead of the HDG scheme to solve the drift-diffusion equatons in order to reduce the computational cost of the optimization. The details of FDM are provided in Ref. 7.

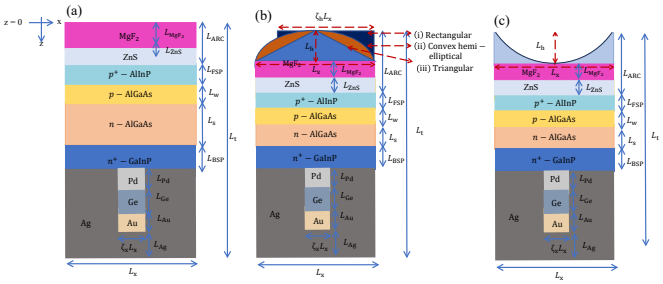

Fig. 1. (a) Schematic of a unit cell of the AlGaAs solar cell. (b) Schematic of the AlGaAs solar cell with periodic surface texturing: (i) rectangular, (ii) convex hemi-elliptical, and (iii) triangular. (c) Schematic of the AlGaAs solar cell with periodic concave hemi-elliptical surface texture. The textured layer of maximum thickness L_h is made of MgF_2.

3. NUMERICAL RESULTS AND DISCUSSION

We begin with $L_h = 0$ so that the front surface of the solar cell is planar. The results on model validation and the effects of the periodically corrugated Ag backreflector combine with localized ohmic Pd–Ge–Au backcontacts on the performance of the solar cells remain unchanged from Part I [1]. Furthermore,

optimal results for solar cells with a homogeneous n-AlGaAs photon-absorbing layer in Part I vary only insignificantly.

A. Optimal solar cells with linear-bandgap grading

We considered the maximization of η when the bandgap of the n-AlGaAs photon-absorbing layer is linearly graded according to Eq. (1) of Part I [1]. Optimization in the same parameter space as in Part I showed that the best linear profile is flat, i.e., no linearly graded photon-absorbing layer yields a higher value of η than the best homogeneous photon-absorbing layer. This conclusion is in contrast to Part I, whose results were affected by the normalization error. However, we caution that this conclusion is not general for all thin-film solar cells, since thin-film CIGS solar cells with a linearly graded photon-absorbing layer have been predicted elsewhere [7] by the same corrected model to perform significantly better than their counterparts with a homogeneous photon-absorbing layer. The optimal results for solar cells with a homogeneous n-AlGaAs layer are provided in Table 1.

B. Optimal solar cells with nonlinear-bandgap grading

We re-optimized η when the bandgap energy $\mathsf{E}_g(z)$ of the n-AlGaAs photon-absorbing layer is nonlinearly graded according to Eq. (2) of Part I [1]; i.e.,

$$\mathsf{E}_g(z) = \mathsf{E}_{g,\min} + A\left(\mathsf{E}_{g,\max} - \mathsf{E}_{g,\min}\right) \times \left\{\frac{1}{2}\left[\sin\left(2\pi K \frac{z-(L_{ARC}+L_{FSP}+L_w)}{L_s} - 2\pi\psi\right)+1\right]\right\}^{\alpha}, \quad z \in [L_{ARC}+L_{FSP}+L_w, L_{ARC}+L_{FSP}+L_w+L_s]\ . \tag{1}$$

Here, $\psi \in [0,1]$ describes a relative phase shift, K is the number of periods in the n-AlGaAs layer, and $\alpha > 0$ is a shaping parameter. The parameter space used for optimizing η was chosen as: $\mathsf{E}_{g,w} \in [1.424, 2.09]$ eV, $\mathsf{E}_{g,\min} \in [1.424, 2.09]$ eV, $\mathsf{E}_{g,\max} \in [1.424, 2.09]$ eV, $A \in [0,1]$, $\alpha \in [0,8]$, $K \in [0,8]$, $\psi \in [0,1]$, $L_x \in [100, 1000]$ nm, and $\zeta \in [0.05, 1]$, where $\mathsf{E}_{g,w}$ is the bandgap energy of the homogeneous p-AlGaAs layer.

Table 1. Predicted parameters of the optimal AlGaAs solar cell with a specified value of $L_s \in [100, 2000]$ nm, when the bandgap of the n-AlGaAs photon-absorbing layer is nonlinearly graded. Note that $\zeta = 0.05$ and $L_h = 0$ for all optimal results presented here.

L_s (nm)	Bandgap type	$\mathsf{E}_{g,w}$ (eV)	$\mathsf{E}_{g,\min}$ (eV)	$\mathsf{E}_{g,\max}$ (eV)	A	α	K	ψ	L_x (nm)	J_{sc} (mA cm^{-2})	V_{oc} (mV)	FF (%)	η (%)	Rel. Enhancement in η (%)
100	Homogeneous	1.424	1.424	-	-	-	-	-	500	19.49	1124	83.63	18.33	
	Nonlinear	1.424	1.424	1.98	0.66	8	0.66	0.65	500	19.33	1131	84.58	18.50	0.92
200	Homogeneous	1.424	1.424	-	-	-	-	-	505	22.99	1123	83.93	21.66	
	Nonlinear	1.424	1.424	1.98	0.66	8	0.66	0.65	505	22.83	1130	85.00	21.94	1.29
300	Homogeneous	1.424	1.424	-	-	-	-	-	502	25.06	1119	84.09	23.59	
	Nonlinear	2.09	1.424	1.98	0.66	8	0.66	0.65	502	23.89	1142	88.31	24.17	2.45
400	Homogeneous	2.09	1.424	-	-	-	-	-	501	25.95	1120	86.15	25.06	
	Nonlinear	2.09	1.424	1.98	1	8	0.66	0.65	501	25.64	1135	88.93	25.89	3.31
500	Homogeneous	2.09	1.424	-	-	-	-	-	500	27.13	1117	86.41	26.19	
	Nonlinear	2.09	1.424	1.98	0.99	8	0.66	0.65	500	26.76	1131	89.04	26.96	2.94
1000	Homogeneous	2.09	1.424	-	-	-	-	-	500	29.34	1104	87.08	28.26	
	Nonlinear	2.09	1.424	1.98	0.66	8	0.66	0.65	500	29.14	1114	88.82	28.88	2.19
2000	Homogeneous	2.09	1.424	-	-	-	-	-	506	30.35	1089	87.66	28.97	
	Nonlinear	2.09	1.424	1.98	0.3	8	0.66	0.65	506	30.14	1096	88.71	29.30	1.14

Values of the short-circuit current density J_{sc}, open-circuit voltage V_{oc}, fill factor FF, and efficiency η predicted by our model are presented in Table 1 for seven different values of L_s, the thickness of n-AlGaAs photon-absorbing layer. The values of $E_{g,w}$, $E_{g,min}$, $E_{g,max}$, A, α, K, ψ, and L_x for the optimal designs are also provided in the same table. Also, the optimal values of the homogeneous-bandgap case are provided in the same table for comparison. Note that optimal values of $L_x \approx 500$ nm and $\zeta = 0.05$ for all the results in Table 1.

For the thinnest n-AlGaAs photon-absorbing layer ($L_s = 100$ nm), the maximum efficiency predicted is 18.50% with $E_{g,w} = 1.424$ eV, $E_{g,min} = 1.424$ eV, $E_{g,max} = 1.98$ eV, $A = 0.66$, $\alpha = 8$, $K = 0.66$, and $\psi = 0.65$. The values of J_{sc}, V_{oc}, and FF corresponding to this optimal design are 19.33 mA cm^{-2}, 1131 mV, and 84.58%, respectively. The relative enhancement of about 1% in η over the optimal homogeneous case (and, *ipso facto*, the linearly graded case) is to be noted.

For the thickest n-AlGaAs photon-absorbing layer ($L_s = 2000$ nm), the maximum efficiency predicted is 29.30% with $E_{g,w} = 2.09$ eV, $E_{g,min} = 1.424$ eV, $E_{g,max} = 1.98$ eV, $A = 0.3$, $\alpha = 8$, $K = 0.66$, and $\psi = 0.65$. The corresponding values of J_{sc}, V_{oc}, and FF are 30.14 mA cm^{-2}, 1096 mV, and 88.71%, respectively. A relative enhancement of 1.14% is predicted with nonlinear grading over over the optimal efficiency of 28.97% with a homogeneous n-AlGaAs photon-absorbing layer.

For $L_s \in [100, 2000]$ nm, the maximum relative enhancement of 3.31% in efficiency with a nonlinearly n-AlGaAs photon-absorbing layer over the homogeneous n-AlGaAs photon-absorbing layer emerges for $L_s = 400$ nm. The maximum efficiency predicted is 25.89% with $E_{g,w} = 2.09$ eV, $E_{g,min} = 1.424$ eV, $E_{g,max} = 1.98$ eV, $A = 1$, $\alpha = 8$, $K = 0.66$, and $\psi = 0.65$. The corresponding values of J_{sc}, V_{oc}, and FF are 25.64 mA cm^{-2}, 1135 mV, and 89.93%, respectively.

We performed a detailed study for the solar cell with the thickest ($L_s = 2000$ nm) nonlinearly graded n-AlGaAs photon-absorbing layer because it delivers the highest efficiency. Spatial profiles of the bandgap energy $E_g(z)$ and electron affinity $\chi(z)$ delivered by optoelectronic optimization are provided in Figs. 2(a) and 2(b), respectively, and those of the conduction band-edge energy $E_c(z)$, valence band-edge energy $E_v(z)$, and intrinsic energy $E_i(z)$ in Fig. 3(a). The spatial variations of E_v and E_i are similar to that of E_g and provide the conditions to enhance the EHP generation rate. Bandgap grading provides large $E_g(z)$ near the p-n junction face of the n-AlGaAs photon-absorbing layer, which elevates V_{oc} [3]. These characteristics are the same as reported in Part I [1]. Figure 3(b) presents the graphs of the electron density $n(z)$, hole density $p(z)$, and intrinsic charge-carrier density $n_i(z)$ under the equilibrium condition. The intrinsic carrier density varies according to the bandgap-energy variation such that it is small where E_g is large and *vice versa*, just as in Part I.

Spatial profiles of $G(z)$ and the EHP recombination rate $R(n, p; z)$ are given in Fig. 4(a). The regions in which $E_g(z)$ is small are of substantial thickness, which is responsible for elevating the EHP generation rate [3]. The nonlinear grading close to the p-n junction face of the n-AlGaAs photon-absorbing layer [shown in Fig. 4(a)] adds a drift field to reduce the recombination rate. These trends are the same as in Part I [1].

The solar cell's J_{dev}–V_{ext} and P–V_{ext} characteristics are shown in Fig. 4(b), with $P = J_{dev}V_{ext}$. From this figure, $J_{dev} = 29.33$ mA cm^{-2}, $V_{ext} = 999$ mV, FF = 88.71%, and $\eta = 29.30\%$ for best performance.

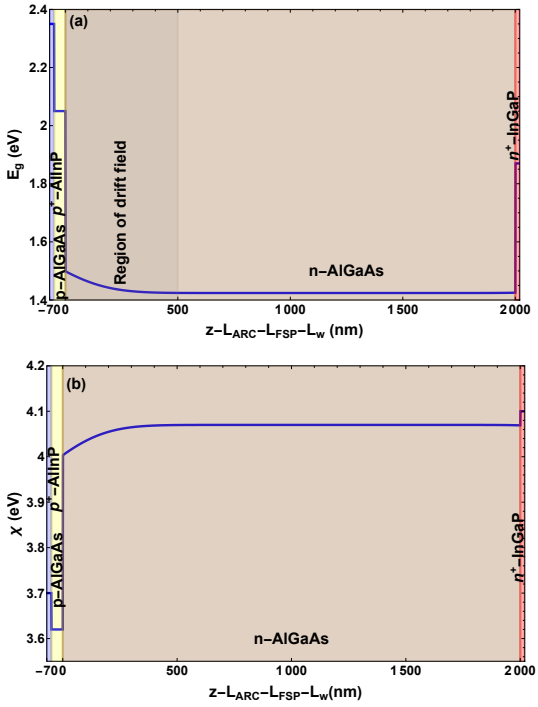

Fig. 2. (a) Spatial profiles of (a) $E_g(z)$ and (b) $\chi(z)$ in the AlInP/p-AlGaAs/n-AlGaAs /InGaP region of the optimal AlGaAs solar cell with a 2000-nm-thick nonlinearly graded bandgap n-AlGaAs layer and a planar front surface ($L_h = 0$).

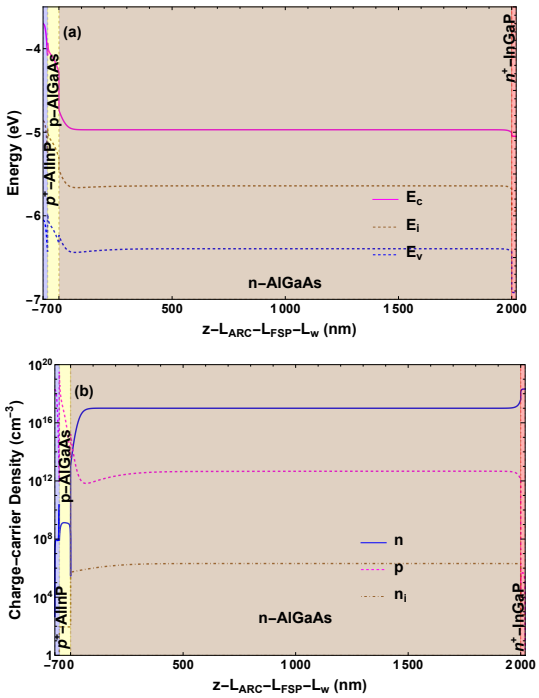

Fig. 3. (a) Spatial profiles of (a) $E_c(z)$, $E_v(z)$, and $E_i(z)$, and (b) $n(z)$, $p(z)$, and $n_i(z)$ in the AlInP/p-AlGaAs/n-AlGaAs /InGaP region of the optimal AlGaAs solar cell with a 2000-nm-thick nonlinearly graded bandgap n-AlGaAs layer and a planar front surface ($L_h = 0$).

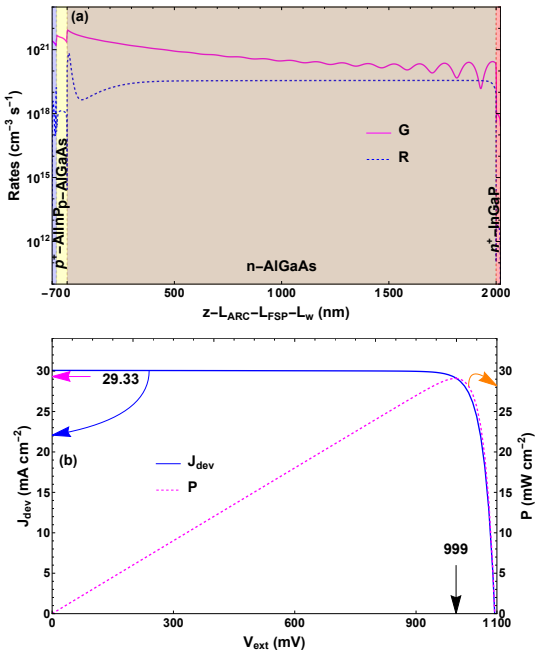

Fig. 4. (a) Spatial profiles of $G(z)$ and $R(n,p;z)$ in the AlInP/p-AlGaAs/n-AlGaAs/InGaP region of the optimal AlGaAs solar cell with a 2000-nm-thick nonlinearly graded bandgap n-AlGaAs layer and a planar front surface ($L_h = 0$). (b) Plots of J_{dev} and P vs. V_{ext} for the same solar cell.

C. Illumination by concentrated sunlight

Next, we analyzed the effects of solar concentration on the efficiency of AlGaAs solar cells. The sunlight-concentration factor is the number c_{sun} of suns, the single-sun spectrum $S(\lambda_0)$ being replaced by $c_{sun}\,S(\lambda_0)$ in the calculation of the EHP generation rate. Since the thickness of thin-film solar cells is on the order of a few micrometers, $c_{sun} \in [1,100]$ was restricted to medium magnitude to avoid detrimental heating effects [10].

C.1. Optimal design

Plots of J_{sc}, V_{oc}, η, and FF of the optimal solar cell with the nonlinearly graded 2000-nm-thick n-AlGaAs layer and a planar front surface ($L_h = 0$) are shown in Fig. 5 as functions of the sunlight-concentration factor $c_{sun} \in [1,100]$. The maximum value of η predicted is 32.70% with $c_{sun} = 100$. The 100-sun efficiency is 11.6% higher than the one-sun efficiency (29.30%). The 100-sun values of J_{sc}, V_{oc}, and FF are 3014.93 mA cm^{-2}, 1221 mV, and 88.84%, respectively.

The linear relationship of J_{sc} with c_{sun} is evident in Fig. 5(a). In contrast, V_{oc} and η in Figs. 5(b) and (c) evince a two-phase trend: as c_{sun} increases from 1 to 100, each of these two parameters increases at a high rate in the first phase, but then at a much slower rate in the second phase. The fill factor shows a three-phase trend: in phase one, FF increases at a high rate; in the second phase, its increases slowly; and in the third phase, it decreases at a moderate rate. These trends are similar to the ones reported earlier [10].

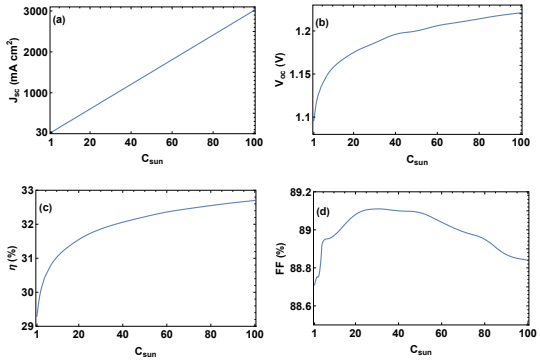

Fig. 5. Plots of (a) J_{sc}, (b) V_{oc}, (c) η, and (d) FF of the optimal thin-film solar cell with a nonlinearly graded-bandgap n-AlGaAs layer of 2000-nm thickness and a planar front surface ($L_h = 0$), as functions of c_{sun}.

The J_{dev}–V_{ext} and P–V_{ext} characteristics of the same solar cell are shown in Fig. 6 for $c_{sun} = 100$. The maximum output power P_{max} delivered is 3270 mW cm^{-2} for $c_{sun} = 100$. Of course, the ratio P_{max}/c_{sun} increases by 11.6% with a hundredfold sunlight concentration, as is expected from the increase of η by the same factor. From this figure, $J_{dev} = 2933$ mA cm^{-2}, $V_{ext} = 1115$ mV, FF = 88.84%, and $\eta = 32.70\%$ for the best performance.

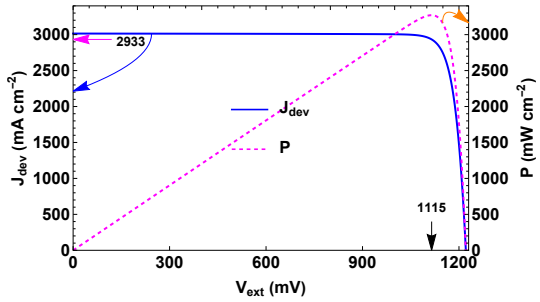

Fig. 6. Plots of J_{dev} and P vs. V_{ext} of the optimal thin-film solar cell with a nonlinearly graded-bandgap AlGaAs layer of 2000-nm thickness and a planar front surface ($L_h = 0$), when $c_{sun} = 100$.

C.2. Effect of sunlight concentration on generation/recombination processes

We also examined the spatial profiles of the c_{sun}-sun EHP generation rate $G_{c_{sun}}(z)$ and the c_{sun}-sun EHP recombination rate $R_{c_{sun}}(n,p;z)$ in order to determine which portions of the semiconductor region are responsible for efficiency enhancement from sunlight concentration. Accordingly, we calculated the values of the net EHP generation rate

$$\gamma_{c_{sun}} = \int_{L_{ARC}}^{L_d} G_{c_{sun}}(z)dz \qquad \textbf{(2a)}$$

and the net EHP recombination rate

$$\rho_{c_{sun}} = \int_{L_{ARC}}^{L_d} R_{c_{sun}}(n,p;z)dz\,, \qquad \textbf{(2b)}$$

where $L_d = L_{ARC} + L_{FSP} + L_w + L_s + L_{BSP}$.

The EHP generation rates $G_{100}(z)$ and $100\,G_1(z)$ are plotted in Fig. 7(a) as functions of z in the semiconductor region of the optimal thin-film solar cell with a nonlinearly graded-bandgap n-AlGaAs layer of 2000 nm thickness. The plots show

that $G_{100}(z) = 100\,G_1(z)$, as expected from the linearity of the optical submodel. Not surprisingly, therefore, $\gamma_{100} = 100\gamma_1 = 1.900 \times 10^{26}$ cm^{-2} s^{-1}.

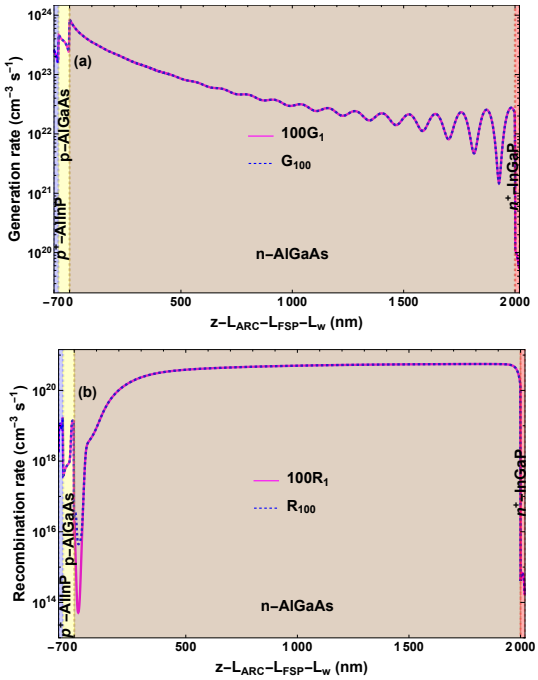

Fig. 7. Spatial profiles of (a) the EHP generation rate and (b) the EHP recombination rate in the semiconductor region of the optimal solar cell with a nonlinearly graded-bandgap AlGaAs layer of 2000-nm thickness and a planar front surface ($L_h = 0$), for the one-sun and 100-sun illumination conditions.

Both $R_{100}(n,p;z)$ and $100\,R_1(n,p;z)$ are plotted as functions of z in the semiconductor regions of the same solar cell in Fig. 7(b). The spatial variation of $R_{100}(n,p;z)$ is similar to that of $100\,R_1(n,p;z)$ in most of the n-AlGaAs layer except near the p-n junction face where $R_{100}(n,p;z) > 100\,R_1(n,p;z)$. The net recombination rates are $100\rho_1 = 8.469 \times 10^{23}$ cm^{-2} s^{-1} and $\rho_{100} = 8.471 \times 10^{23}$ cm^{-2} s^{-1}, which show that the per-sun recombination rate remains almost unchanged on exposure to concentrated sunlight. Hence, the improvement of V_{oc} due to higher J_{sc} is the major reason for the efficiency enhancement since V_{oc} is proportional to $\ln(1 + J_{sc}/J_{dark})$ for ideal photodiodes, where J_{dark} is the dark current density; see Eq. (1.6) of Ref. 4.

D. Optimal periodic front-surface texturing

We considered the design of an AlGaAs solar cell with four different types of periodic front-surface texturing shown in Fig. 1(b): (i) rectangular, (ii) convex hemi-elliptical, (iii) triangular, and (iv) concave hemi-elliptical. The hemi-elliptical profile is given by

$$\left(\frac{x}{L_x}\right)^2 + \left(\frac{z}{L_h}\right)^2 = 1\,. \tag{3}$$

The textured layer of maximum thickness L_h was taken to be composed of MgF_2. The solar cell was taken to contain either a homogeneous-bandgap or a nonlinearly graded-bandgap photon-absorbing layer, with $L_s \in \{200, 1000, 2000\}$ nm, $\zeta = 0.05$, and the bandgap energy fixed as in Table 1. In the case of rectangular texturing, the duty cycle $\zeta_h \in [0,1]$ was also considered as an optimization parameter.

D.1. Rectangular texturing

First, we considered optimizing the rectangular texturing. The parameter space for optimizing η was chosen as: $L_h \in [1,1000]$ nm, $L_x \in [100,1000]$ nm, $\zeta_h \in [0,1]$, $L_{MgF_2} \in [1,1000]$ nm, and $L_{ZnS} \in [1,1000]$ nm. Optimal combinations of the values of L_h, L_x, ζ_h, L_{MgF_2}, and L_{ZnS} are recorded in Table 2, along with the corresponding values of J_{sc}, V_{oc}, FF, and η.

Ultrathin n-AlGaAs layer. When $L_s = 200$ nm, the maximum efficiency predicted with the optimal homogeneous n-AlGaAs photon-absorbing layer is 21.90% with $L_h = 30$ nm, $L_x = 600$ nm, $\zeta_h = 0.75$, $L_{MgF_2} = 82$ nm, and $L_{ZnS} = 50$ nm. A relative enhancement of 1.10% over the value of 21.66% for a planar front surface ($L_h = 0$) is predicted. The short-circuit current density increased from 22.99 mA cm^{-2} to 23.26 mA cm^{-2} due to the reduction of front reflection via surface texturing, but both V_{oc} and FF were not affected much by surface texturing.

The maximum efficiency predicted with the optimal nonlinearly graded-bandgap n-AlGaAs photon-absorbing layer is 22.20% with $L_h = 30$ nm, $L_x = 600$ nm, $\zeta_h = 0.75$, $L_{MgF_2} = 70$ nm, and $L_{ZnS} = 50$ nm. A relative enhancement of 1.18% over the planar-front-surface value of 21.94% should be noted.

Table 2 shows that the maximum thickness $L_h + L_{MgF_2}$ of MgF_2 and the thickness L_{ZnS} of ZnS are affected by about 10% by texturing. More remarkably, $L_x = 600$ nm is optimal when the front surface is periodically textured, but $L_x = 505$ nm is optimal when the front surface is planar ($L_h = 0$); accordingly, the use of Pd, Ge, and Au is predicted to reduce by about 20% and the use of Ag to concomitantly increase due to front-surface texturing.

Intermediate-thickness n-AlGaAs layer. When $L_s = 1000$ nm, the maximum efficiency predicted with the optimal homogeneous photon-absorbing layer is 28.40% with $L_h = 30$ nm, $L_x = 600$ nm, $\zeta_h = 0.75$, $L_{MgF_2} = 70$ nm, and $L_{ZnS} = 50$ nm. A relative enhancement of 0.49% over the value of 28.26% for a planar front surface ($L_h = 0$) is indicated. V_{oc} remains unchanged, and the enhancement is mainly due to increased EHP generation rate because of reduced front reflection.

The maximum efficiency predicted with the optimal nonlinearly graded-bandgap n-AlGaAs layer is 29.02% with the same set of bandgap-energy parameters as in Table 1. A relative enhancement of 0.48% over the planar-front-surface value of 28.88% is found.

Thus, the relative enhancement in maximum efficiency due to periodic front-surface texturing decreases when a thicker photon-absorbing layer is considered. The amounts of MgF_2, ZnS, Pd, Ge, Au, and Ag either increase or decrease with front-surface texturing.

Standard-thickness n-AlGaAs layer. Finally, we set $L_s = 2000$ nm. Whether the bandgap-energy profile of the n-AlGaAs is uniform or nonlinearly graded, periodic front-surface texturing does enhance the maximum efficiency, according to Table 2. But the relative enhancement is even weaker than for $L_s = 1000$ nm. Even so, periodic front-surface texturing reduces the amount of MgF_2; increases the amount of ZnS; and either reduces (homogeneous n-AlGaAs) or increases (graded-bandgap n-AlGaAs) the amounts of Pd, Ge, and Au, with concomitant changes in the usage of Ag.

D.2. Convex hemispherical and triangular texturing

With convex hemi-elliptical or triangular texturing of the front surface, the efficiency trend is similar to that for rectangular texturing, according to Table 2. Periodic front-surface texturing delivers a small relative enhancement in efficiency over the

planar front surface, and the enhancement is lower when the n-AlGaAs layer is thicker.

Since the period L_x increases for the ultrathin n-AlGaAs layer on front-surface texturing, the amounts of Pd, Ge, and Au decrease and the amount of Ag increases. In contrast, front-surface texturing leads to a decrease in the period L_x when the n-AlGaAs layer is thicker, the amounts of Pd, Ge, and Au increase and the amount of Ag decreases. The amounts of both MgF_2 and ZnS are also affected somewhat due to front-surface texturing.

D.3. Concave hemispherical texturing

Lastly, we considered optimizing the concave hemi-elliptical texturing shown in Fig. 1(c). The parameter space for optimizing η was chosen as: $L_h \in [1, 1000]$ nm, $L_x \in [100, 1000]$ nm, $L_{MgF_2} \in [1, 1000]$ nm, and $L_{ZnS} \in [1, 1000]$ nm. Optimal combinations of the values of L_h, L_x, L_{MgF_2}, and L_{ZnS} are recorded in Table 2, along with the corresponding values of J_{sc}, V_{oc}, FF, and η.

Ultrathin n-AlGaAs layer. When $L_s = 200$ nm, the maximum efficiency predicted with the optimal homogeneous n-AlGaAs photon-absorbing layer is 22.13% with $L_h = 30$ nm, $L_x = 600$ nm, $L_{MgF_2} = 82$ nm, and $L_{ZnS} = 50$ nm. A relative enhancement of 2.16% over the value of 21.66% for a planar front surface is predicted. The maximum efficiency predicted with the optimal nonlinearly graded-bandgap n-AlGaAs photon-absorbing layer is 22.45% with $L_h = 30$ nm, $L_x = 600$ nm, $L_{MgF_2} = 82$ nm, and $L_{ZnS} = 50$ nm. A relative enhancement of 2.32% over the planar-front-surface value of 21.94% should be noted.

Intermediate-thickness n-AlGaAs layer. When $L_s = 1000$ nm, the maximum efficiency predicted with the optimal homogeneous photon-absorbing layer is 28.37% with $L_h = 30$ nm, $L_x = 600$ nm, $L_{MgF_2} = 82$ nm, and $L_{ZnS} = 50$ nm. A relative enhancement of 0.38% over the value of 28.26% for a planar front surface ($L_h = 0$) is indicated. V_{oc} remains unchanged, and the enhancement is mainly due to increased EHP generation rate because of reduced front reflection. The maximum efficiency predicted with the optimal nonlinearly graded-bandgap n-AlGaAs layer is 29.00% with the same set of bandgap-energy parameters as in Table 1. A relative enhancement of 0.41% over the planar-front-surface value of 28.88% is found.

Standard-thickness n-AlGaAs layer. Finally, we set $L_s = 2000$ nm. The relative enhancement is even weaker than for $L_s = 1000$ nm. The maximum efficiency predicted with the optimal homogeneous photon-absorbing layer is 29.01% with $L_h = 25$ nm, $L_x = 400$ nm, $L_{MgF_2} = 82$ nm, and $L_{ZnS} = 50$ nm. A relative enhancement of 0.13% over the value of 28.97% for a planar front surface ($L_h = 0$) is indicated. The maximum efficiency predicted with the optimal nonlinearly graded-bandgap n-AlGaAs layer is 29.37% with the same set of bandgap-energy parameters as in Table 1. A relative enhancement of 0.24% over the planar-front-surface value of 29.30% is found.

According to Table 2, the concave hemi-elliptical texturing performs slightly better than the rectangular texturing, convex hemi-elliptical, and triangular texturing when $L_s = 200$ nm, but not for $L_s \in \{1000, 2000\}$ nm. Also, the amounts of MgF_2 and ZnS either increase or decrease with front-surface texturing.

D.4. To texture or not to texture?

Hence, a decision on whether or not to periodically texture the front surface on the scale of 0.5–2 free-space wavelengths depends on: (i) the cost of the texturing process, (ii) the texture profile, (iii) the magnitude of relative enhancement of efficiency for the specific thickness of the photon-absorbing layer and (iv) the concomitant reductions and increases of diverse materials above and below the semiconductor region of the solar cell. Financial considerations would be necessary in making the right choice [30], all the more so since front-surface texturing would not increase the efficiency by more than ∼2.32% over the planar-front-surface efficiency.

4. CONCLUDING REMARKS

We optimized AlGaAs solar cells containing an n-AlGaAs photon-absorbing layer with either (i) homogeneous bandgap, (ii) linearly graded bandgap, or (iii) nonlinearly graded bandgap. The positive effects of the periodically corrugated Ag backreflector along with localized ohmic Pd–Ge–Au backcontacts on the performance of the AlGaAs solar cells and the optimal results for solar cells with a homogeneous n-AlGaAs photon-absorbing layer in Part I [1] remain unchanged and hence are not reported here. Furthermore, we optimized the geometrical parameters of three different types of periodic front-surface texturing to reduce loss due to reflection.

Our new algorithm for the electrical submodel confirmed that optimal bandgap grading enhances the power-conversion efficiency by as much as 3.31% when the n-AlGaAs photon-absorbing layer is 400-nm-thick and 1.14% when the n-AlGaAs photon-absorbing layer is 2000-nm-thick. These efficiency enhancements are lower than those reported in Part I due to specifics on the short-circuit current density and the open-circuit voltage affected by the normalization error. Bandgap grading provides the condition of large $\mathsf{E}_g(z)$ in the proximity of the plane p-n junction (which elevates V_{oc}), and there are regions in the photon-absorbing layer wherein $\mathsf{E}_g(z)$ is small (which elevates the EHP generation rate); both of these characteristics are similar to those reported in Part I. Furthermore, a relative efficiency increase by an additional 11.6% is possible if sunlight was concentrated a hundredfold.

Periodic texturing of the front surface on the scale of 0.5–2 free-space wavelengths provides a small relative enhancement in efficiency when compared the planar front surface, the enhancement being lower when the n-AlGaAs layer is thicker. However, resulting changes in material usage and the cost of texturing should be factored in, before deciding against front-surface texturing.

Acknowledgments. A. Lakhtakia thanks the Charles Godfrey Binder Endowment at the Pennsylvania State University for ongoing support of his research. The research of F. Ahmad and A. Lakhtakia was partially supported by U.S. National Science Foundation (NSF) under grant number DMS-2011996. The research of P. B. Monk was supported by U.S. NSF under grant number DMS-2011603.

Funding. US National Science Foundation (DMS-2011996 and DMS-2011603)

Disclosures. The authors declare no conflicts of interest.

Table 2. Predicted parameters of the optimal AlGaAs solar cell with a specified value of $L_s \in \{200, 1000, 2000\}$ nm, when (i) the n-AlGaAs photon-absorbing layer is either homogeneous or nonlinearly graded with the bandgap energy fixed as in Table 1. and (ii) the front surface is periodically textured. Whereas $\zeta = 0.05$ is fixed, $L_s \in \{200, 1000, 2000\}$ nm.

L_s/Bandgap (nm)/-	Texturing type	L_h (nm)	L_x (nm)	ζ_h (nm)	L_{MgF_2} (nm)	L_{ZnS} (nm)	J_{sc} (mA cm^{-2})	V_{oc} (mV)	FF (%)	η (%)	Rel. Enhancement in η (%)
200/Homogeneous	Planar	0	505	-	110	40	22.99	1123	83.93	21.66	
	Rectangular	30	600	0.75	82	50	23.26	1122	83.90	21.90	1.10
	Convex hemi-elliptical	30	600	-	82	50	23.26	1122	83.90	21.90	1.10
	Triangular	50	600	-	82	50	23.23	1122	83.90	21.87	0.96
	Concave hemi-elliptical	30	600	-	82	50	23.50	1122	83.89	22.13	2.16
200/Nonlinear	Planar	0	505	-	110	40	22.83	1130	85.00	21.94	
	Rectangular	30	600	0.75	70	50	23.11	1130	85.03	22.20	1.18
	Convex hemi-elliptical	30	600	-	82	50	23.11	1130	85.03	22.20	1.18
	Triangular	30	600	-	70	50	23.08	1130	85.03	22.17	0.95
	Concave hemi-elliptical	30	600	-	82	50	23.37	1130	85.01	22.45	2.32
1000/Homogeneous	Planar	0	500	-	110	40	29.34	1104	87.08	28.26	
	Rectangular	30	600	0.75	70	50	29.58	1103	87.04	28.40	0.49
	Convex hemi-elliptical	35	400	-	90	50	29.58	1103	87.14	28.44	0.64
	Triangular	35	400	-	90	50	29.62	1103	8703	28.45	0.67
	Concave hemi-elliptical	30	600	-	82	50	29.49	1103	87.18	28.37	0.38
1000/Nonlinear	Planar	0	500	-	110	40	29.14	1114	88.82	28.88	
	Rectangular	30	600	0.75	70	50	29.32	1113	88.93	29.02	0.48
	Convex hemi-elliptical	35	400	-	90	50	29.39	1113	88.85	29.07	0.66
	Triangular	35	400	-	90	50	29.39	1113	88.85	29.07	0.66
	Concave hemi-elliptical	30	600	-	82	50	29.27	1113	88.99	29.00	0.41
2000/Homogeneous	Planar	0	506	-	110	40	30.35	1089	87.66	28.97	
	Rectangular	30	600	0.75	70	50	30.41	1088	87.61	28.98	0.03
	Convex hemi-elliptical	50	200	-	82	50	30.51	1088	87.53	29.06	0.31
	Triangular	50	200	-	82	50	30.47	1088	87.56	29.03	0.21
	Concave hemi-elliptical	25	400	-	82	50	30.45	1088	87.56	29.01	0.13
2000/Nonlinear	Planar	0	506	-	110	40	30.14	1096	88.71	29.30	
	Rectangular	30	400	0.75	70	50	30.24	1094	88.68	29.34	0.14

Convex hemi-elliptical	35	400	-	90	50	30.32	1094	88.53	29.37	0.24
Triangular	50	150	-	82	50	30.45	1095	88.37	29.47	0.58
Concave hemi-elliptical	25	400	-	82	50	30.29	1095	88.57	29.37	0.24

REFERENCES

1. F. Ahmad, A. Lakhtakia, and P. B. Monk, "Optoelectronic optimization of graded-bandgap thin-film AlGaAs solar cells," *Appl. Opt.* **59**, 1018-1027 (2020).
2. F. Ahmad, A. Lakhtakia, and P. B. Monk, *Theory of Graded-Bandgap Thin-Film Solar Cells* (Morgan & Claypool, 2021).
3. S. J. Fonash, *Solar Cell Device Physics* (Academic, 2010).
4. J. Nelson, *The Physics of Solar Cells* (Imperial College, 2003).
5. D. Brinkman, K. Fellner, P. A. Markowich, and M.-T. Wolfram, "A drift-diffusion-reaction model for excitonic photovoltaic bilayers: asymptotic analysis and a 2-D HDG finite-element scheme," *Math. Models Methods Appl. Sci.* **23**, 839–872 (2013).
6. R. J. LeVeque, *Finite Difference Methods for Ordinary and Partial Differential Equations: Steady State and Time Dependent Problems* (SIAM, 2007).
7. F. Ahmad, A. Lakhtakia, B. J. Civilletti, and P. B. Monk, "Efficiency enhancement of ultrathin CIGS solar cells by optimal bandgap grading. Part II: finite-difference algorithm and double-layer antireflection coatings," *Appl. Opt.* **61**, 10049–10061 (2022).
8. F. Dimroth, T. N. D. Tibbits, M. Niemeyer, F. Predan, P. Beutel, C. Karcher, E. Oliva, G. Siefer, D. Lackner, P. Fuß-Kailuweit, A. W. Bett, R. Krause, C. Drazek, E. Guiot, J. Wasselin, A. Tauzin, and T. Signamarcheix, "Four-junction wafer-bonded concentrator solar cells," *IEEE J. Photovolt.* **6** 343–349 (2016).
9. M. A. Green, "Photovoltaic technology and visions for the future," *Prog. Energy* **1**, 013001 (2019).
10. F. Ahmad, A. Lakhtakia, and P. B. Monk, "Enhanced efficiency of graded-bandgap thin-film solar cells due to concentrated sunlight," *Appl. Opt.* **60**, 10570–10578 (2021).
11. H. K. Raut, V. A. Ganesh, A. S. Nair, and S. Ramakrishna, "Anti-reflective coatings: A critical, in-depth review," *Energy Environ. Sci.* **4**, 3779–3804 (2011).
12. J. Zhao and M. A. Green, "Optimized antireflection coatings for high-efficiency silicon solar cells," *IEEE Trans. Electron Devices* **38**, 1925–1934 (2011).
13. F. Chen and L. Wang, *Light Trapping Design in Silicon-Based Solar Cells* (INTECH, 2011).
14. P. W. Baumeister, *Optical Coating Technology* (SPIE, 2004).
15. W. H. Southwell, "Pyramid-array surface-relief structures producing antireflection index matching on optical surfaces," *J. Opt. Soc. Am. A* **8**, 549–553 (1991).
16. S. A. Boden and D. M. Bagnall, "Optimization of moth-eye antireflection schemes for silicon solar cells," *Prog. Photovolt. Res. Appl.* **18**, 195–203 (2010).
17. J. Cai and L. Qi, "Recent advances in antireflective surfaces based on nanostructure arrays," *Mater. Horiz.* **2**, 37–53 (2015).
18. N. Yamada, T. Ijiro, E. Okamoto, K. Hayashi, and H. Masuda, "Optimization of anti-reflection moth-eye structures for use in crystalline silicon solar cells," *Opt. Express* **19**, A118–A125 (2011).
19. L. Chen, W. Qingkang, W. Peihua, H. Kun, and S. Xiangqian, "Light trapping characteristics of glass substrate with hemisphere pit arrays in thin film Si solar cells," *Chin. Phys. B* **24**, 040202 (2015).
20. L. Chen, B. Fang, Q. Ke, P. Wangyang, K. Hu, and W. Zhang, "Quasi-hemispherical pit array textured surface for increasing the efficiency of thin film solar cells," *AIP Adv.* **12**, 015111 (2022).
21. F. Chiadini, V. Fiumara, A. Scaglione, and A. Lakhtakia, "Bioinspired pit texturing of silicon solar cell surfaces," *J. Photon. Energy* **3**, 034596 (2013).
22. P. Campbell and M. A. Green, "High performance light trapping textures for monocrystalline silicon solar cells," *Sol. Energ. Mater. Sol. Cell.* **65**, 369–375 (2001).
23. P. Verlinden, O. Evrard, E. Mazy, and A. Crahay, "The surface texturization of solar cells: a new method using V-grooves with controllable sidewall angles," *Sol. Energ. Mater. Sol. Cell.* **26**, 71–78 (1992).
24. P. K. Pal, S. K. Datta, K. Mukhopadhyay, and H. Saha "Role of antireflection coating in microgrooved silicon solar cells," *Sol. Energ. Mater. Sol. Cell.* **43**, 1–14 (1996).
25. M. Python , E. Vallat-Sauvain, J. Bailat, D. Dominé, L. Fesquet, A. Shah, and C. Ballif, "Relation between substrate surface morphology and microcrystalline silicon solar cell performance," *J. Non-Cryst. Solids* **354**, 2258–2262 (2008).
26. A. Lakhtakia and S. Ashok, "Analysis of textured surfaces for photovoltaics," *Sol. Energ. Mater. Sol. Cell.* **46**, 137–146 (1997).
27. Y. Saito, O. Yamaoka, and A. Yoshida, "Plasmaless etching of silicon using chlorine trifluoride," *J. Vac. Sci. Technol. B* **9**, 2503–2506 (1991).
28. G Kumaravelu, M. M Alkaisi, A Bittar, D. Macdonald, and J Zhao, "Damage studies in dry etched textured silicon surfaces," *Curr. Appl. Phys.* **4**, 108–110 (2004).
29. M. G. Moharam, D. A. Pommet, E. B. Grann, and T. K. Gaylord, "Stable implementation of the rigorous coupled-wave analysis for surface-relief gratings: enhanced transmittance matrix approach," *J. Opt. Soc. Am. A* **12**, 1077–1086 (1995).
30. K. A. W. Horowitz, T. Remo, B. Smith, and A. Ptak, *A Techno-Economic Analysis and Cost Reduction Roadmap for III-V Solar Cells*, Technical Report NREL/TP-6A20-72103 (NREL, 2018).